Engineering Fracture Mechanics 289 (2023) 109414

Contents lists available at ScienceDirect

Engineering Fracture Mechanics

journal homepage: www.elsevier.com/locate/engfracmech

Influence of hydrogen on the hydraulic fracture behavior of a 42CrMo4 steel welds: Effect of the prior austenite grain size

L.B. Peral [a,b,*], A. Díaz [a], V. Arniella [b], J. Belzunce [b], J.M. Alegre [a], I.I. Cuesta [a]

[a] Universidad de Burgos, Structural Integrity Research Group, Escuela Politécnica Superior, Avenida Cantabria s/n, Burgos 09006, España
[b] Universidad de Oviedo. SIMUMECAMAT Research Group, Escuela Politécnica Superior de Ingeniería de Gijón, Gijón 33203, España

ARTICLE INFO

Keywords:
High internal pressure
PAGS
Hydrogen cathodic precharge
Martensitic lath decohesion
hydrogen embrittlement

ABSTRACT

The influence of hydrogen on the mechanical behavior of a quenched and tempered 42CrMo4 steel has been evaluated by means of high internal pressure fracture tests carried out on hydrogen precharged notched cylindrical specimens. The notched cylindrical specimens were precharged in a 1 M H_2SO_4 + 0.25 g/l As_2O_3 solution for 3 h with 1.2 mA/cm^2. Hydraulic fracture tests were performed at different loading rates. Hydrogen embrittlement resistance increased with grain size refinement although the fine grained specimen had a higher hydrogen content than the coarse grained one. Fractographic analysis showed hydrogen enhanced decohesion fracture was less pronounced with decreasing grain size. Hydrogen embrittlement susceptibility is discussed in terms of the prior austenite grain size (PAGS) and the operative fracture mechanisms.

1. Introduction

For the upcoming new hydrogen economy society, vessels and pipelines used to store and transport hydrogen must be able to provide a safe service during long periods of time [1]. Therefore, it is essential to ensure a good resistance to hydrogen embrittlement (HE). HE is a phenomenon responsible for premature failure of metallic materials that can take place when hydrogen atoms diffuse into these metallic components submitted to static and cyclic mechanical loads in hydrogen environment.

Pipelines, operating at pressure up to 13 MPa, have been commonly manufactured with API 5L X42 to X52 steel grades [2]. However, the suitability of using higher pipeline steel grades such us API 5L X70 to X80 is nowadays in progress to acommodate higher pressure of hydrogen to satisfy the growing energy demand in a cost-effective way. In the short term, natural gas pipelines will be employed to carry natural gas mixed with hydrogen whilst 100% hydrogen should be distributed in the long term [3]. In this regard, Nguyen et al. [4] have studied the hydrogen embrittlement susceptibility of a X70 pipeline steel under various gas mixture conditions (CH_4-H_2). In order to deal with high hydrogen pressures, up to 90 or even 115 MPa [5,6], high strength Cr-Mo steel grades are also promising economical candidates for hydrogen distribution and storage in hydrogen refueling stations [7]. It is important to recall that the severity of HE usually increases with increasing hydrogen pressure [8]. In this sense, quenched and tempered Cr-Mo steels are commonly used when a good combination of strength and toughness is required. Bending and welding heavy steel rolled plates represent a cost-effective way to produce high capacity pressure vessels to contain high pressure hydrogen gas. However, it is well known that the applied thermal cycles during the welding process have a notable effect on the microstructure of the heat-affected zone

* Corresponding author at: Universidad de Burgos, Structural Integrity Research Group, Escuela Politécnica Superior, Avenida Cantabria s/n, Burgos 09006, España.
E-mail addresses: lbperal@ubu.es, luisborja@uniovi.es (L.B. Peral).

https://doi.org/10.1016/j.engfracmech.2023.109414
Received 28 February 2023; Received in revised form 9 May 2023; Accepted 7 June 2023
Available online 12 June 2023

Table 1
Binding energy (E_b) intervals in kJ/mol.

Microstructural feature	E_b (kJ/mol)	Ref
TiC	46–116	[17]
NbC	82/63–68	[18]/[19]
Dislocation cores	56–58	[20,21]
High-angle grain boundary	47–59	[22–24]
Precipitated VC, V_4C_3	33–35	[25,26]
Elastic-field of dislocation	20–30	[20,27]
Martensitic lath, blocks and packets interfaces	17	[25,27]
$(Fe, Cr, Mo)_3C$	11–13	[21,27]

Table 2
Chemical composition (% wt.).

Fe	C	Mn	Si	Cr	Mo
balance	0.42	0.62	0.18	0.98	0.22

(HAZ), that is the region of the weld with the lowest toughness. Hence, this region is especially sensitive to hydrogen damage [9,10].

The effect of hydrogen on mechanical properties of different quenched and tempered martensitic microstructures has been widely studied in literature, considering both fracture [11–14] and fatigue [1,5,9,15,16] properties. The interaction between hydrogen and steel microstructure plays a big role in order to explain the hydrogen embrittlement susceptibility in quenched and tempered steels. Hydrogen diffusion, including hydrogen trapping and detrapping phenomena, is dominated by specific microstructural sites, known as 'traps' (Table 1).

These microstructural trapping sites can be characterized as reversible or irreversible depending on their hydrogen trapping capability [20,28]. This fact underlines that hydrogen states (i.e. lattice, reversible and irreversible trapped hydrogen) are key factors in the hydrogen-enhanced degradation, demonstrating the important role that microstructural features can play on the embrittlement process [25,29].

The prior austenite grain size (PAGS) influences hydrogen embrittlement behavior [30]. Control of the microstructural size scale is one key aspect in order to develop a hydrogen-resistant martensitic steel. Microstructural refinement seems to be beneficial for the resistance of a lath martensitic steel to hydrogen embrittlement. In this regard, L. Cho et al. [31] studied the effects of hydrogen pressure and PAGS on the hydrogen embrittlement characteristics of a press-hardened martensitic steel. They reported that martensite with smaller prior austenite grain size is more resistant to gaseous HE. Martiniano et al. [32] also analyzed the role of PAGS on hydrogen embrittlement susceptibility of a modified AISI 4130 steel. The microstructure with the smallest PAGS (4.94 μm) evidenced the lowest hydrogen embrittlement susceptibility in comparison to a microstructure with a PAGS of 27.12 μm. Due to the finer PAGS, a higher fraction of high angle grain boundaries (HAGBs) was determined. HAGBs are irreversible hydrogen trapping sites (Table 1) which retain part of the diffusible hydrogen, slowing down its movement towards the potential crack nucleation sites. S. Chen et al. [33] studied the effect of grain size on the hydrogen embrittlement sensitivity of a precipitation strengthened Fe-Ni based alloy. The results evidenced that hydrogen embrittlement susceptibility was reduced with decreasing grain size from 95 to 32 μm. Besides, fractographic analysis showed that intergranular fracture was less pronounced with decreasing grain size. Similar observations were also reported in [32,34].

On the other hand, Nakamura and Furubayashi [35] reported that the crack propagation rate in gaseous hydrogen in a tempered martensitic sample was slower when the PAGS was larger, what improves hydrogen resistance with increasing PAGS from 45 to 450 μm. A similar effect was reported by Lessar and Gerberich [36]. In this case, they postulated that the improvement was because higher austenitizing temperatures induce the formation of retained austenite, which can act as a hydrogen-trapping site. The beneficial effect of retained austenite is often explained by its low hydrogen diffusivity [37]. The contradicting results are possibly because of several secondary parameters associated with the microstructural changes such as: alloying elements, strength level, hydrogen absorption and desorption capability, dislocation density, residual austenite content and test conditions (i.e. hydrogen charging methodology). To shed light on these contradictory theories, the mechanical behavior of a low carbon steel, with two different PAGS, has been studied in the presence of internal hydrogen. Besides, the novelty of this work is focused on the use of high-pressure hydraulic fracture tests that have not been commonly employed by the scientific community in the last years To reduce hydrogen precharging time, miniature cylindrical samples were employed. With this geometry, a biaxial stress state, similar to that found in a thin-walled cylinder submitted to high pressure, can be reproduced to evaluate hydrogen embrittlement susceptibility.

Hydrogen embrittlement susceptibility of a quenched and tempered 42CrMo4 steel with a PAGS of 20 μm (BS) has been studied at different loading rates by hydraulic fracture tests at high internal pressure, in the presence of internal hydrogen (ex-situ tests). Results are compared with those obtained in the same steel grade, but in this case, with a PAGS of 150 μm [11] that simulates the coarse grain heat affected zone (CGHAZ), as explained later. Trapping and diffusivity features are also characterized by means of thermal desorption analysis (TDA) and numerical modelling approaches.

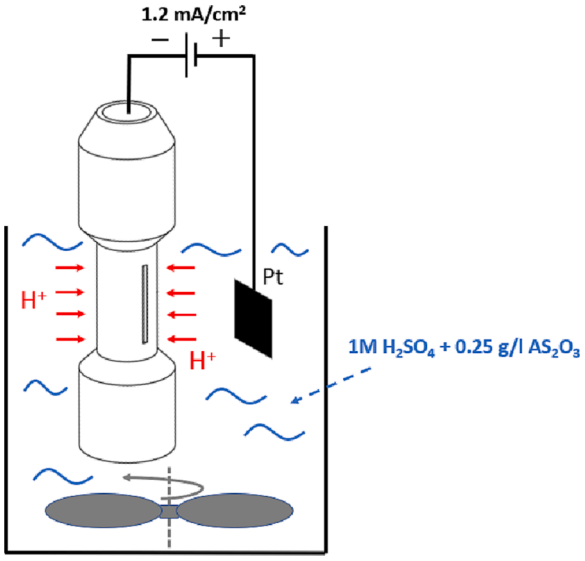

Fig. 1. Experimental set up. Hydrogen precharging method.

2. Material and experimental procedure

2.1. Material and heat treatments

A low-alloyed ferritic steel (42CrMo4 grade, AISI4140) has been employed in this study. The chemical composition, in weight %, is given in Table 2.

Hot-rolled plates of 250×250×12 mm^3 were austenitized at 845 °C for 45 min, quenched in water and finally, tempered at 700 °C for 2 h. This grade was denoted as base steel (BS). Additionally, in order to simulate, at the laboratory scale, the coarse grain of the heat affected zone of a weld, 42CrMo4 plates of 250×125×12 mm^3 were also austenitized at 1200 °C for 20 min, followed by an oil quenching and then, tempered also at 700 °C for 2 h to simulate a post-welding heat treatment (PWHT). For more information on the weld characterization and the simulation process of the CGHAZ, the reader is addressed to [38].

2.2. Hydrogen electrochemical precharge

Specimens, corresponding to BS and simulated CGHAZ, were electrochemically precharged at room temperature with a current density of 1.2 mA/cm^2 for 3 h time, in a 1 M H_2SO_4 + 0.25 g/l AS_2O_3 solution, with a pH around 1. As_2O_3 addition hinders hydrogen atoms recombination on the surface of the metal and a higher hydrogen content can be attained in the specimen. Similar H-precharging conditions were also employed in [13]. The experimental set up is illustrated in Fig. 1. Moderate agitation was used during the H-charging process.

2.3. Hydrogen desorption at RT

Plates of 30 mm length, 11 mm width and 2 mm thickness were machined to analyze the hydrogen desorption curve at room temperature for each grain size condition. Thin plates (BS and simulated HAZ) were cathodically charged in a 1 M H_2SO_4 + 0.25 g/l AS_2O_3 solution, following the process described in section 2.2.

Hydrogen concentration (wt ppm) was measured by Thermal Desorption Analysis (TDA) by means of a LECO DH603 hydrogen analyser, maintaining the thin plates at 1100 °C for 300 s [25]. Hydrogen concentration (C_{H0}) was immediately measured after the hydrogen precharge. Besides, some of the charged thin plates were also exposed to air, after precharging, at different intervals of time: 2, 4 and 24 h, respectively. Before starting the measure, each sample was cleaned in an ultrasonic bath with acetone for 5 min, and then carefully dried using cold air. Diffusivity and trapping features are fitted from the experimental desorption curve at room temperature, considering two different numerical modelling approaches (section 2.4), to assess the loading rate effect (i.e. ramp of pressure) on embrittlement.

2.4. Numerical modelling of hydrogen desorption

In order to evaluate the loading rate effect on embrittlement, diffusivity and trapping features are fitted from the experimental desorption curve at room temperature, considering two different numerical modelling approaches. Both of them are implemented in the *transport of diluted species* module in the Finite Element software Comsol Multiphysics.

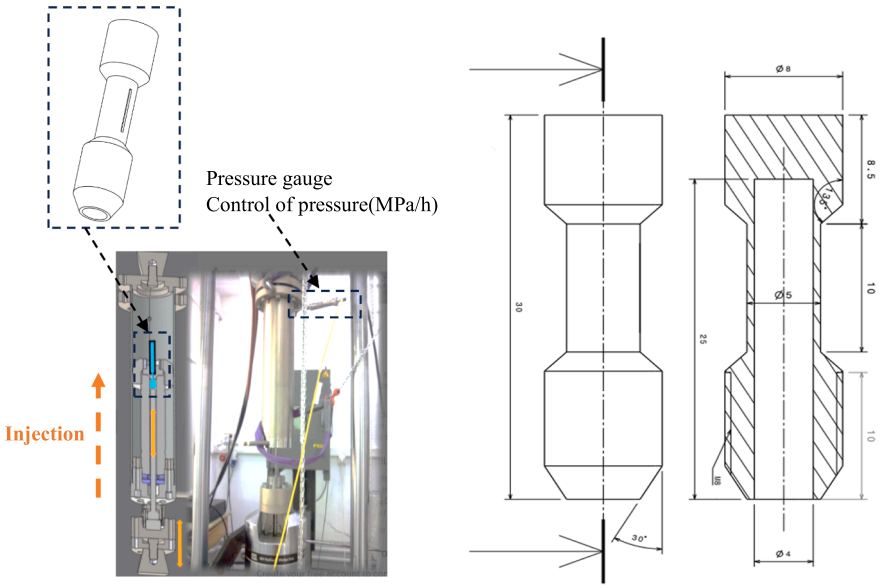

Fig. 2. (a) Experimental set-up. (b) Notched cylindrical specimen (dimensions in mm).

The simulated geometry is a 3D model of the steel plate of $30\times11\times2$ mm^3; mesh consists of hexahedral linear elements including 20 elements in the thickness direction, i.e. the direction that controls diffusion during desorption, with a biased distribution in order to obtain a finer mesh near the surface where the concentration gradients are higher.

2.4.1. Apparent diffusivity modelling

A constant and apparent diffusivity D_{app} can be assumed, and the mass diffusion equation is simplified as follows:

$$\frac{\partial C}{\partial t} = D_{app}\nabla^2 C \tag{1}$$

where C is the total hydrogen concentration at each specimen point. In this approach, hydrogen content measured just after pre-charging represents the initial condition, whereas trapped hydrogen that remains after 24 h (C_{Hirrev}) is fixed as the boundary condition for the exit surface following the approach from [39].[40]

$$C(\mathbf{x}, t=0) = C_{H0} \tag{2}$$

$$C(\mathbf{x}\in\mathscr{S}, t) = C_{H,24} \tag{3}$$

where $\mathbf{x}$ represents the point coordinates and $\mathscr{S}$ the sample boundary. Fixing initial and boundary conditions from experimental results, D_{app} is obtained by iterating over different values and choosing the curve that minimises the sum of square residuals R at 2 and 4 h.

$$R = \sum_{t=2,4}\left(\overline{C}_t - C_{H,t}\right)^2 \tag{4}$$

$\overline{C}_t$ is obtained by integration over the 3D specimen at time t and $C_{H,t}$ is the corresponding experimental value measured after room temperature desorption.

However, D_{app} does not depend on local concentration in contrast to experimental observations and theoretical demonstrations. A more sophisticated trapping model is required to capture different diffusion regimes depending on the concentration range.

2.4.2. Two-level modelling

Total concentration C can be divided into two species: hydrogen in lattice sites, C_L, and hydrogen in traps, C_T. This two-level strategy has been adopted by many authors for the study of trapping kinetics and hydrogen transport phenomena near a crack tip [40]. Hydrogen flux is here only determined by lattice diffusion, where D_L is the ideal diffusion coefficient:

$$\frac{\partial C_L}{\partial t} + \frac{\partial C_T}{\partial t} = D_L\nabla^2 C_L \tag{5}$$

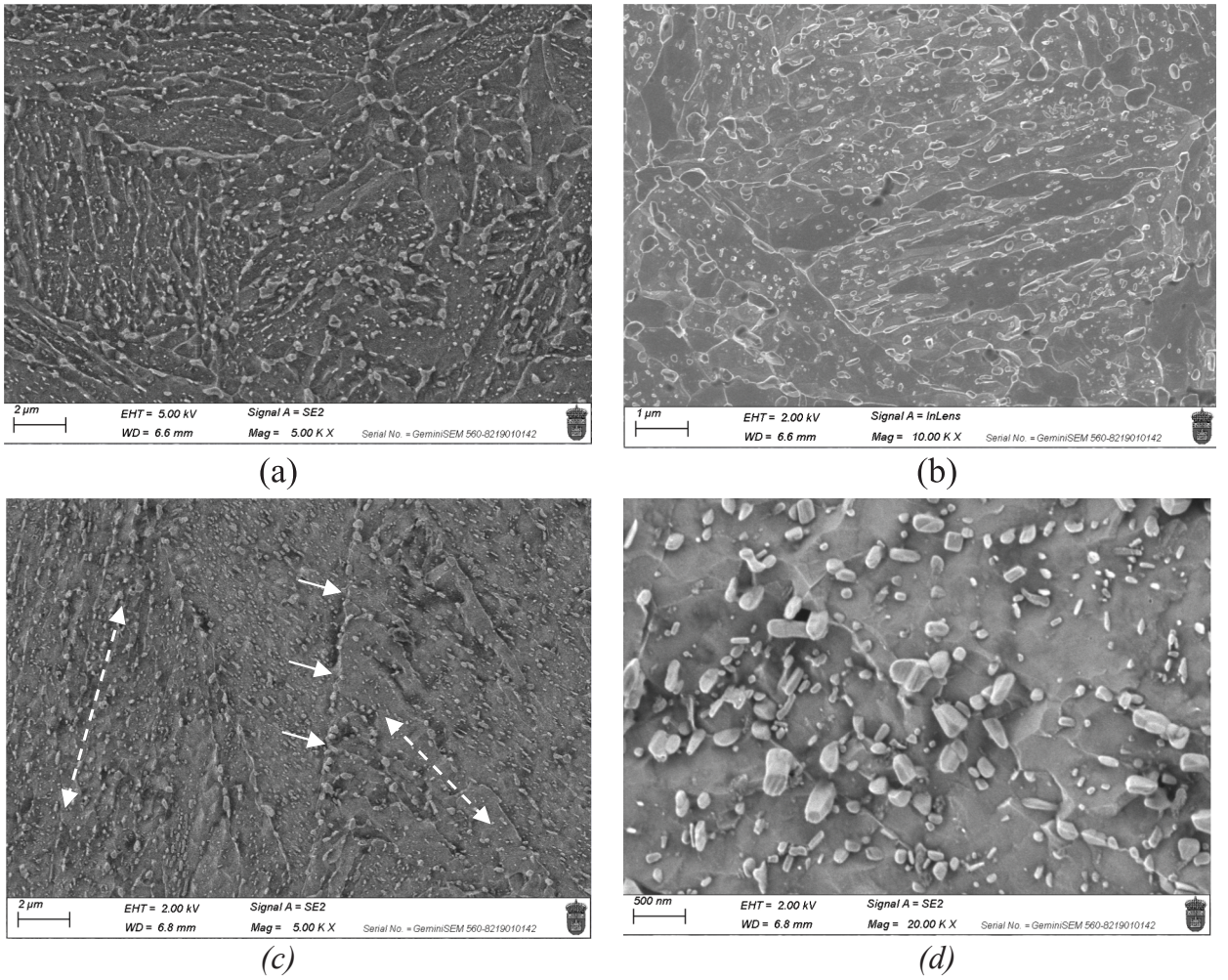

Fig. 3. 42CrMo4 microstructure. (a, b) BS grade and (c, d) CGHAZ grade whit white arrows pointing the grain boundary and the dotted white arrows pointing along the martensitic lath interfaces.

Table 3
Mechanical properties [38]. HV: hardness Vickers, σ_{ys}: yield strength, σ_{uts}: ultimate tensile strength and A: elongation.

	HV_{30}	σ_{ys} (MPa)	σ_{uts} (MPa)	A (%)
BS (PAGS ≈ 20 µm)	207	622	710	23
CGHAZ (PAGS ≈ 150 µm)	230	600	750	24

Assuming thermodynamic equilibrium, the trapping rate can be expressed in terms of C_L and two trap parameters: the binding energy of defects, E_b, and the density of trapping sites, N_T. Applying the chain rule and operating as in [41]:

$$\frac{\partial C_L}{\partial t} = D_L \nabla^2 C_L - \frac{\frac{K_T N_T}{N_L}}{\left[1 + \frac{C_L}{N_L}(K_T - 1)\right]^2} \frac{\partial C_L}{\partial t} \tag{6}$$

where $K_T = \exp(E_b/RT)$, being R the constant of gases and T the temperature. N_L and N_T represent density of lattice and trapping sites, respectively. Trapping rate is simulated in Comsol Multiphysics including the last term of Eq. (6) as a reaction term. A zero-concentration boundary condition is now applied to C_L to model instantaneous exit, whereas the initial condition is fixed as $C_L(\mathbf{x}, t = 0) = \widehat{C}_0 - C_{T,0}$, where $C_{T,0}$ is found assuming thermodynamic equilibrium in this approach, D_L must be assumed from theoretical or experimental data. Here, $D_L = 6{\times}10^{-10}$ m^2/s is used following the value obtained by Peral et al. [42]. The residual now is calculated also including the experimental value at 24 h, since the boundary condition is not dependent on that value.

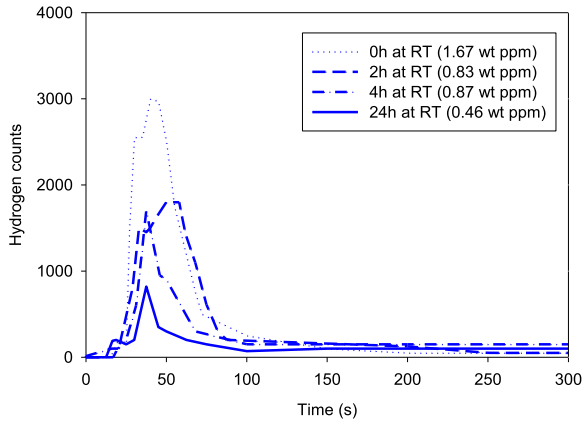

(a)

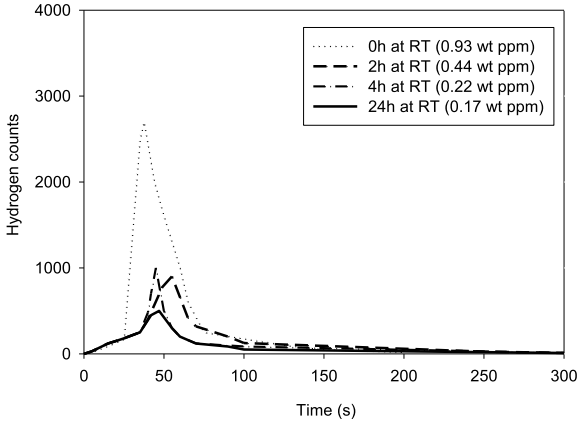

(b)

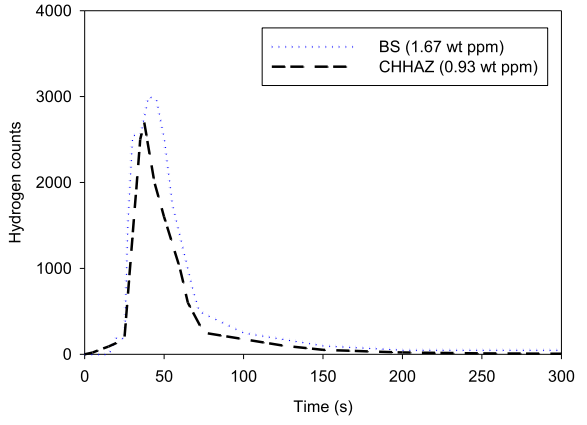

(c)

Fig. 4. Thermal desorption analysis. (a) TDA profiles for BS. (b) TDA profiles for CGHAZ [11]. (c) Initial hydrogen content in the BS and CGHAZ steel.

$$R = \sum_{t=2,4,24} \left(\overline{C}_t - C_{H,t}\right)^2 \tag{7}$$

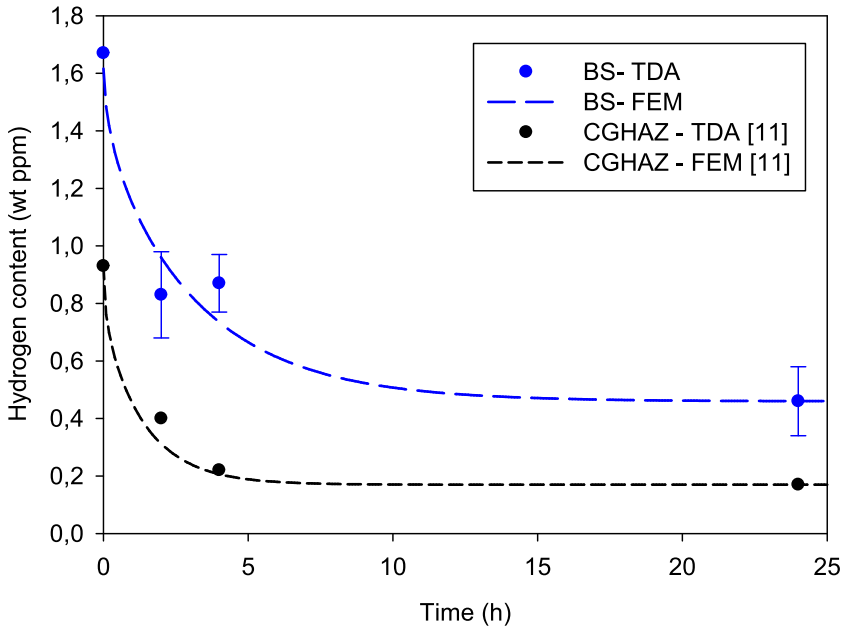

Fig. 5. Hydrogen desorption curves at RT and data fitting.

Table 4
H-microstructure interaction.

42CrMo4	C_{H0} (wt ppm)	C_{Hirrev} (wt ppm)	C_{Hdif}		D_{app} (m^2/s)	N_T (sites/m^3)	E_b (kJ/mol)
			(wt ppm)	(%)			
BS	1.67	0.46	1.21	72	$3{\cdot}10^{-11}$	$5{\cdot}10^{24}$	45
CGHAZ	0.93	0.17	0.76	82	$7{\cdot}10^{-11}$	$2{\cdot}10^{24}$	48

2.5. Hydraulic fracture tests

Hydraulic fracture tests have been carried out in a high-pressure test device, able to attain 6000 bar of internal pressure. Hydraulic fracture tests were performed by means of a piston that is controlled by a MTS820 machine, Fig. 2a. Water was injected at high pressure, from 25 to 7000 MPa/h, until the burst pressure (P_b') is reached. Fig. 2b displays the geometry of the notched cylindrical specimens employed in this study.

A longitudinal notch of 250 μm depth, 60° angle and tip radius less than 0.1 mm was machined. The ideal ligament length is approximately 250 μm.

The burst pressure (P_b') was corrected by Eq. (8), where P_b is the corrected burst pressure and P_b' represents the experimental burst pressure at the moment of failure. K_{ideal} (Eq. (9)) and K_{real} (Eq. (10)) are the correction factors. $\varnothing_i$ is the internal diameter of the notched miniature cylindrical specimen and b (in Eq. (10)) is the final ligament length that was measured by the scanning electron microscope (SEM) after testing. The ideal ligament length is 0.25 mm, Eq. (9).

$$P_b = P_b^{'} \frac{K_{ideal}^2}{K_{real}^2} \tag{8}$$

$$K_{ideal} = \frac{\varnothing_i + 2 \cdot 0.25}{\varnothing_i} \tag{9}$$

$$K_{real} = \frac{\varnothing_i + 2 \cdot b}{\varnothing_i} \tag{10}$$

2.6. Observation of microstructures and fracture surfaces

The BS and the simulated coarser HAZ microstructures were observed in a scanning electron microscope JEOL JSM-6460LV, using an acceleration voltage of 2–5 kV. The samples were previously ground and finally polished with 1 μm diamond paste and etched with Nital-2%. The fracture surfaces of the fracture-tested specimens were also carefully examined using the same technique, using an

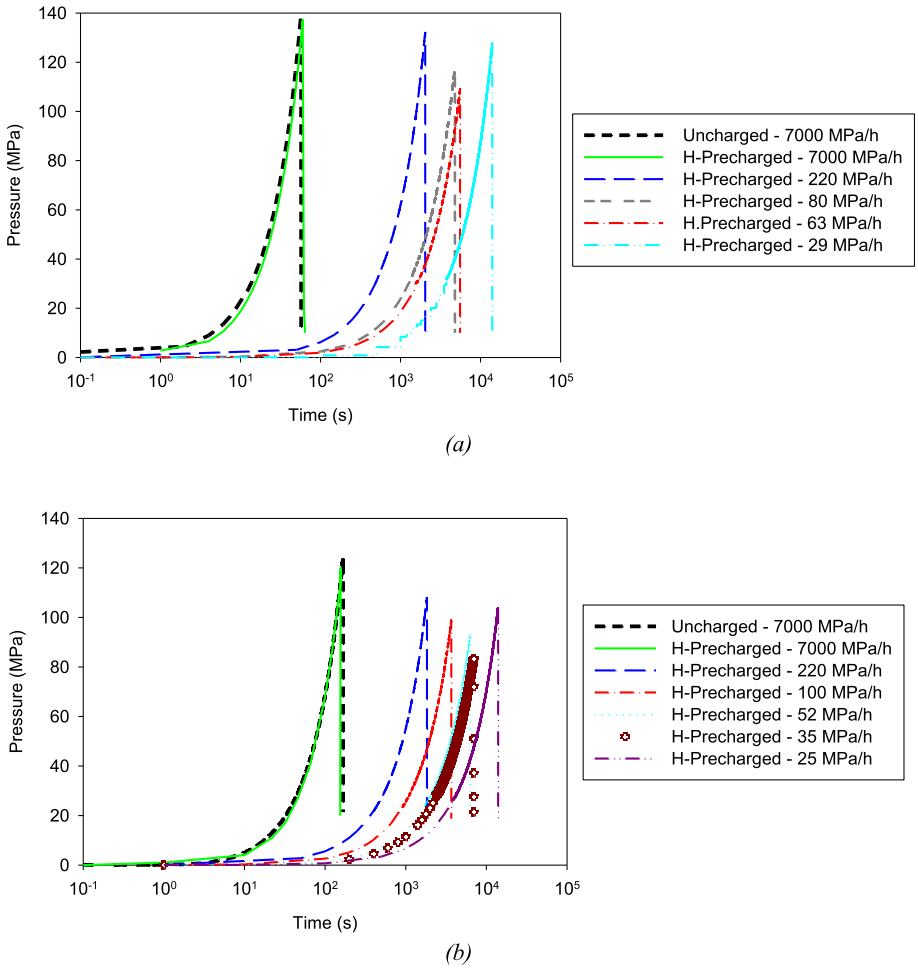

Fig. 6. Hydraulic fracture tests curves. (a) BS grade. (b) CGHAZ grade.

Table 5
Hydraulic fracture tests results. BS with a PAGS of 20 μm and simulated CGHAZ with a PAGS of 150 μm.

		V_{test} (MPa/h)	Test duration (s)	P_b (MPa)	NMOD (mm)
BS	Uncharged	7000	57	137 ± 7	1.91
	H-precharged	7000	62	134	1.90
		220	2030	132	1.70 ± 0.025
		80	4777	118 ± 5	1.47 ± 0.05
		63	5560	109 ± 6	1.59 ± 0.1
		29	14,000	128 ± 3	1.78 ± 0.035
CGHAZ	Uncharged	7000	167	115 ± 10	1.98
	H-precharged	7000	150	112	1.97
		220	1842	108	1.67
		100	3690	99	1.51
		52	5752	91 ± 3	1.33 ± 0.16
		35	6994	83	1.00
		25	15,000	100 ± 5	1.66

Table 6
Embrittlement indexes (EI) and fracture micromechanisms by order of importance. *MVC: microvoid coalescence, CMD: carbides-matrix interfaces decohesion and PRHIC: Plasticity related hydrogen induced cracking. Embrittlement Index: EI (%) $=\frac{X_{no-H}-X_H}{X_{no-H}}\cdot 100$.

	V_{test} (MPa/h)	EI P_b (%)	EI NMOD (%)	*Fracture micromechanism
BS	7000	2	1	MVC
	220	2	11.2	MVC
	80	12	23.1	MVC + CMD/QC
	63	18	17.0	MVC + CMD/QC + PRHIC (40 μm)
	29	5	6.6	MVC + CMD/QC
CGHAZ	7000	3	1	MVC
	220	6	16	MVC
	100	14	24	MVC + CMD + PRHIC
	52	20	33	MVC + PRHIC (60 μm) + CMD
	35	28	50	MVC + PRHIC (80 μm) + CMD/QC + microcracks
	25	13	16	MVC + CMD

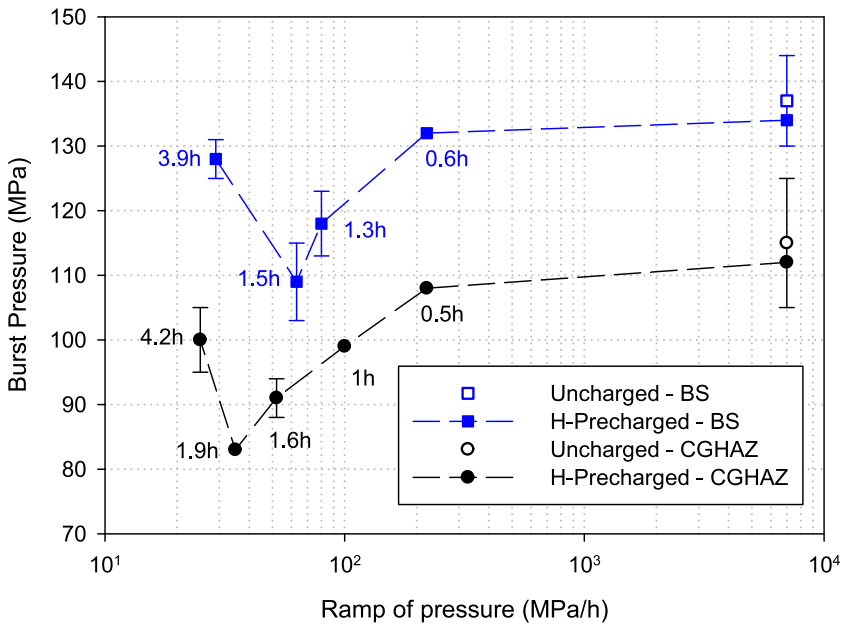

Fig. 7. Burst pressure evolution in the presence of internal hydrogen for the different ramps of pressure (MPa/h) in a 42CrMo4 steel grade with two different PAGS.

acceleration voltage of 20 kV.

3. Results and discussion

3.1. Microstructure

The obtained microstructures after the described heat treatments are displayed in Fig. 3. Regarding the BS microstructure, it is shown in Fig. 3a and b and it corresponds to tempered martensite with a PAGS of 20 ± 5 μm (which was measured in the as-quenched) and a hardness level of 207 HV. The profuse carbide precipitation that takes place during the tempering treatment can be clearly distinguished. Coarse globular and lenticular carbides precipitate along the PAGB while the smallest ones are evenly distributed inside the martensitic laths. EDX analysis revealed that carbides are mainly Fe-rich and they accommodate significant amounts of Cr (12%). In the case of the simulated coarser HAZ, a PAGS of 150 μm (as-quenched condition) was determined with a hardness level of 230 HV. A profuse carbide precipitation (Fig. 3c and d) can be also observed along the PAGB (indicated with white arrows) and martensitic lath interfaces (indicated with dotted white arrows). Carbides are Fe-rich and they have been previously identified as Fe_3C [11]. This grade was denoted as coarse grain, simulating the heat affected zone (CGHAZ).

Mechanical properties of these steel grades after the aforementioned heat treatments are given in Table 3.

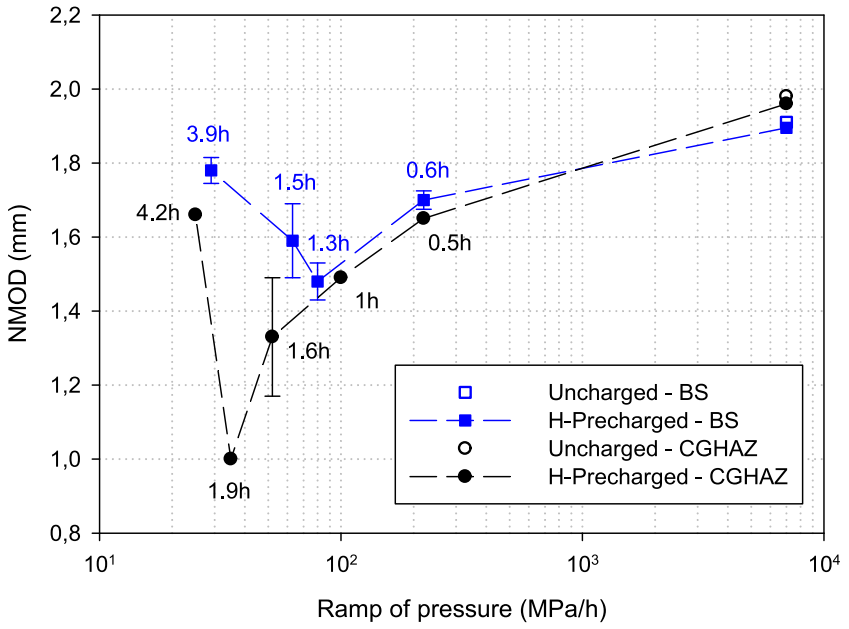

Fig. 8. NMOD evolution in the presence of internal hydrogen for the different ramps of pressure (MPa/h) in a 42CrMo4 steel grade with two different PAGS.

3.2. Hydrogen desorption at RT

Fig. 4 shows the thermal desorption profiles obtained in the BS (Fig. 4a) and CGHAZ (Fig. 4b) grades. Hydrogen content was measured by means of a LECO DH603 hydrogen analyzer, after the precharging methodology described in chapter 2.2 and 2.3. In order to know hydrogen desorption at room temperature (RT), some of the samples were exposed in air for 2, 4 and 24 h. The initial hydrogen content (0 h at RT) introduced into the samples is also compared in Fig. 4c.

Hydrogen content introduced in the BS (PAGS – 20 μm) was 1.67 wt ppm while in the CGHAZ (PAGS – 150 μm) a hydrogen concentration of 0.93 wt ppm was measured. Hydrogen desorption curves at room temperature (RT) are given in Fig. 5. The initial hydrogen content, C_{H0}, corresponds to the first point of the curve (t = 0). The residual hydrogen, C_{Hirrev}, is the hydrogen content that is strongly trapped in the steel microstructure after a long exposure at room temperature. Diffusible hydrogen ($C_{H0} - C_{Hirrev}$) is the amount that is able to escape from traps and diffuse out of the steel (C_{Hdif}). These values are summarized in Table 4. In the same table, the apparent diffusivity (D_{app}), the density of traps (N_T) and the binding energy (E_b) are also showed. These parameters have been calculated by the data fitting carried out from the experimental hydrogen desorption curves (Fig. 5) and both numerical modelling approaches described above.

Irreversible hydrogen content (C_{Hirrev}) increased in the BS grade. Hence, a higher hydrogen concentration remained strongly trapped in the microstructure after a long time (0.46 wt ppm). Grain boundary density is higher in the BS grade because of its smaller PAGS. Due to this fact, the density of traps (N_T – $5{\cdot}10^{24}$ sites/m^3) is considerably higher while the apparent diffusivity is lower (D_{app} – $3{\cdot}10^{-11}$). N_T values in the range of 10^{23} to 10^{26} sites/m^3 have been reported in the literature for martensitic steels [28]. In this study, the estimated binding energy (E_b – 45–48 kJ/mol) has been mainly associated to hydrogen strongly trapped along the HAGBs [22–24,43] and cannot be attributed to different trapping features between BS and CGHAZ. However, it is important to recall that this hydrogen trapped would also include trapped hydrogen at vacancies and dislocations accumulated at HAGBs [44].

Although their study was conducted by hydrogen electrochemical permeation tests instead of TDA analysis, Zhang et al. [45] also reported that the microstructural refinement of a martensitic steel result in a substantial increase in the hydrogen solubility but a significant decrease in the effective hydrogen diffusivity, what has been also observed in the present study. According to this, Fuchigami et al. [46] showed that a martensitic steel with a smaller PAGS (i.e. higher density of hydrogen trapping sites) absorbs a greater hydrogen concentration as a consecuence of the increased boundary area.

3.3. Hydraulic fracture tests

Fig. 6 displays the variation of the pressure registered as a function of the time for the uncharged and hydrogen precharged notched specimens, with two different PAGS (i.e. BS and simulated CGHAZ).

The burst pressure (P_b) and the notch mouth opening displacement (NMOD) are given in Table 5 for the applied ramps of pressure (MPa/h). In the same table, test duration, util the moment of failure, is also indicated.

The embrittlement indexes (EI) related to the burst pressure (P_b) and NMOD are shown in Table 6 for both grades of steel: BS (PAGS

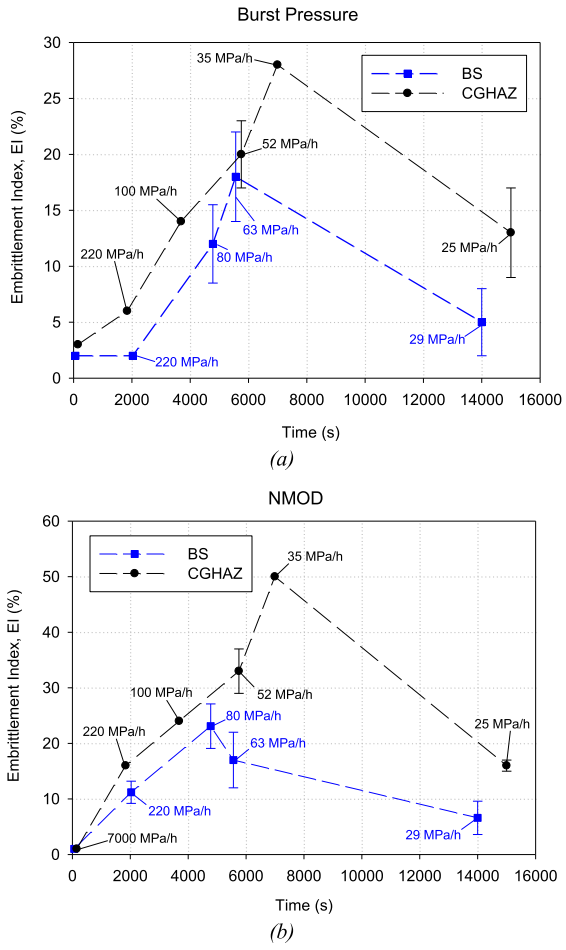

Fig. 9. Influence of the prior austenite grain size (PAGS) on the hydrogen embrittlement. (a) Burst pressure. (b) NMOD. The loading rate is indicated inside the figure.

– 20 μm) and the simulated CGHAZ (PAGS – 150 μm). The operative fracture micromechanisms, later shown in section 3.4, are also indicated by order of importance.

Hydrogen embrittlement indexes (EI) are dependent on the applied ramp of pressure (i.e. test duration). Hydrogen damage increases as test duration increases (i.e. as ramp of pressure decreases) and it is especially noted in the CGHAZ grade for test time of 1.5–2 h. However, in both grades hydrogen embrittlement is partially alleviated for test times higher than 2 h. Presumably, after 3–4 h testing, due to hydrogen diffusivity at room temperature, most diffusible hydrogen has already diffused out of specimens (Fig. 7). The burst pressure and the NMOD variation, as a function of the applied ramp of pressure, is also displayed in Fig. 7 and Fig. 8, respectively. The test duration, in hours, is also indicate in the same figures.

3.4. Effect of PAGS on hydrogen embrittlement and fracture micromechanisms

Fig. 9(a and b) shows the embrittlement indexes trend related to the burst pressure (P_b) and the notch mouth opening displacement (NMOD), respectively. In this figure, embrittlement index is represented as a function of the time at failure, which is dependent of the pressure ramp (i.e. loading rate). As mentioned, hydrogen embrittlement susceptibility has diminished by decreasing the PAGS. The embrittlement trends are consistent with the observed fracture micromechanisms.

The most representative fracture surfaces, corresponding to the uncharged and maximum embrittlement condition, for each steel grade, are shown in Fig. 10. The NMOD reduction due to internal hydrogen effect can be directly noted on these fracture surfaces.

Fig. 11 illustrates the fracture micromechanism corresponding to the BS uncharged specimen (P_b = 137 MPa and NMOD = 1.91 mm) which consists in the initiation, growth and coalescence of microvoids, MVC. A similar fracture micromechanism was also observed in the uncharged coarse grain specimen.

For more details related to fracture micromechanims observed in the coarse grain the reader is addressed to [11]. Focusing now in the BS hydrogen precharged specimens, tested at 80 MPa/h, internal hydrogen effect was already clearly noted (Fig. 12). Two different regions were observed on the fracture surface. The first one, with a 200 μm depth, was distinguished in the region closest to the notch

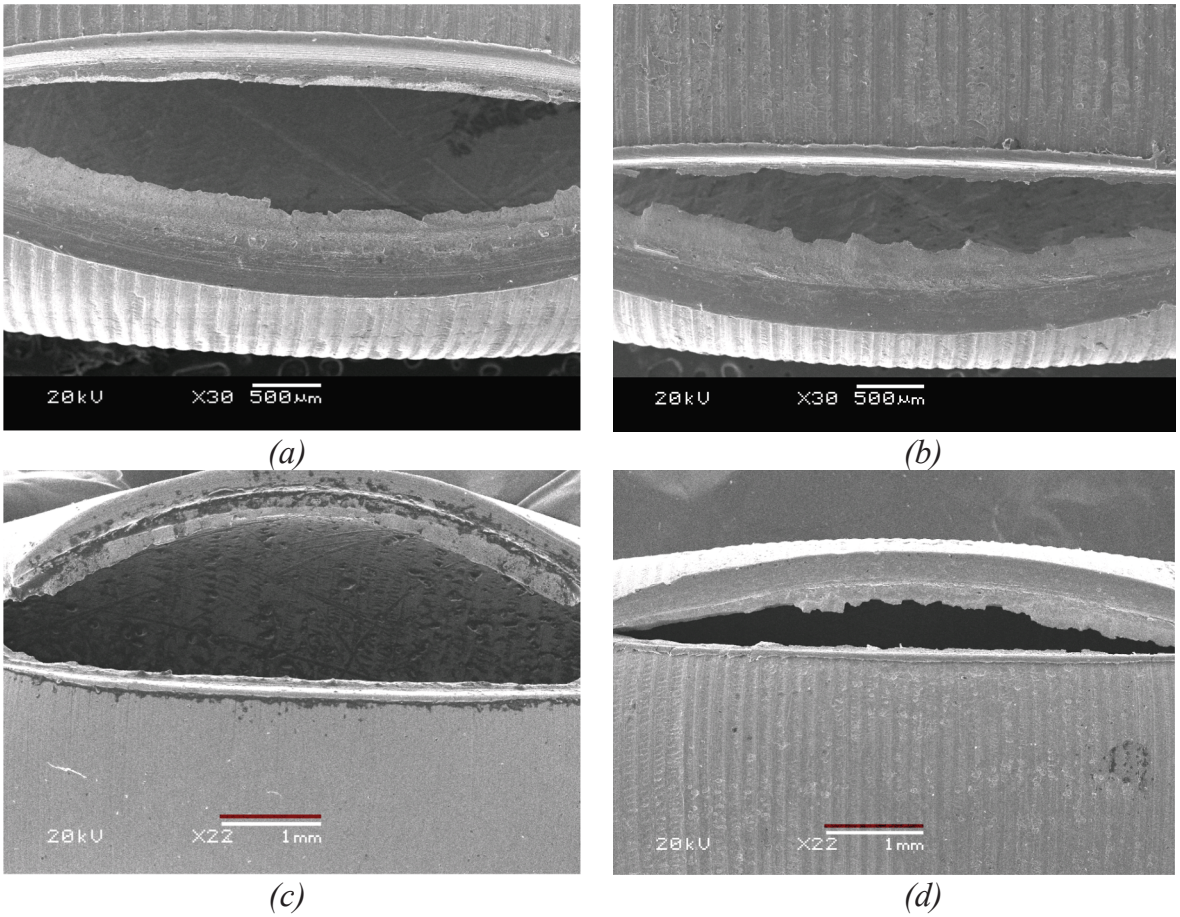

Fig. 10. Representative fracture surfaces. (a) Uncharged specimen and (b) Hydrogen precharged and tested 63 MPa/h in the BS. (c) Uncharged specimen and (d) Hydrogen precharged and tested 35 MPa/h in the CGHAZ.

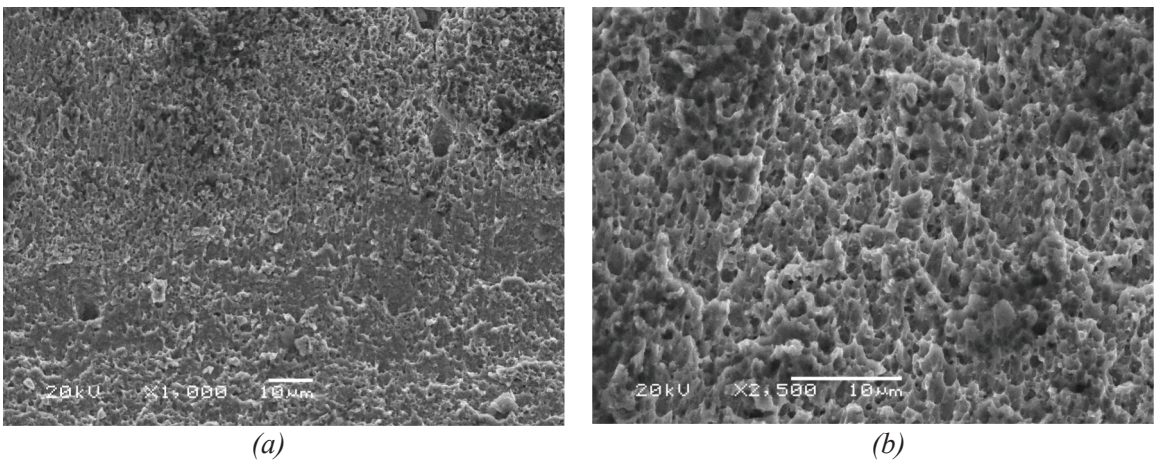

Fig. 11. Uncharged specimen. Coalescence of microvoids at different magnification 1000x (a) and 2500x (b). 42CrMo4 with a PAGS of 20 µm (BS grade).

tip area. This region has the appearance of a quasi-cleavage (QC) where very small dimples are also observed. These small dimples (Fig. 12b) correspond to the carbide-matrix interfaces decohesion, CMD [38,47]. The second area corresponds to the final fracture region and it is characterized by the MVC micromechanism.

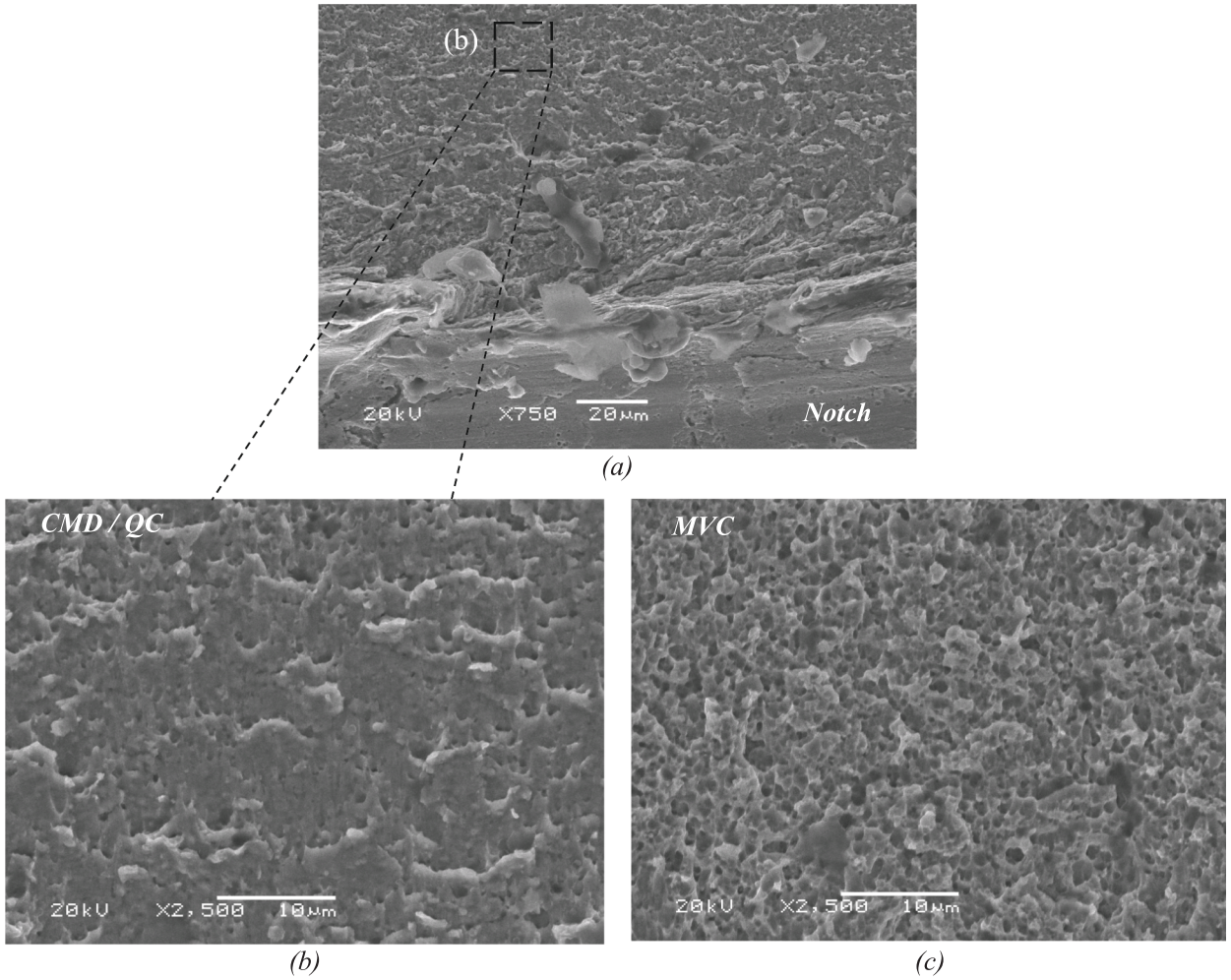

Fig. 12. Hydrogen precharged specimen and tested at 80 MPa/h. (a) General fracture surface appearance near the notch region. (b) Carbide matrix decohesion interfaces. (c) Coalescence of microvoids corresponding to the final fracture of the specimen. 42CrMo4 steel with a PAGS of 20 μm (BS grade).

Fracture micromechanisms in the presence of internal hydrogen are detailed in Fig. 13 for the BS grade, tested at 63 MPa/h. On the general fracture surface, three different regions can be noted (Fig. 13a). Near the notched region, a belt, with approximately 40–50 μm depth, was observed and it is characterized by ductile micro-plastic tearing on a very fine scale, along the martensitic packets, blocks an laths interfaces (Fig. 13b). This micromechanism is commonly known as PRHIC (plasticity related hydrogen induced cracking) in quenched and tempered steel grades [48]. In a more remote region from the notch, very small dimples, with an average size about of 0.5 μm, were seen. This micromechanism, with a depth of 100 μm in the contiguous area to the PRHIC (Fig. 13a), is produced because of the decohesion along the carbides-matrix interfaces (CMD in Fig. 13c and d). The size of these dimples (0.5 μm) is comparable in dimensions to the Fe-Cr rich carbides precipitated during the tempering treatment [11,49].

MVC was finally observed in the bulk of the specimen (Fig. 13e). It is important to mention that the CMD micromechanism was also noted in specimens tested at 80 MPa/h in the presence of hydrogen. However, at 80 MPa/h PRHIC micromechanism was not clearly observed.

In the BS grade, hydrogen embrittlement was mainly observed after 1.3–1.5 h testing. In this regard, we postulate that hydrogen diffusivity ($3{\cdot}10^{-11}$ m^2/s) is mainly coupled with test speed, at 80 and 63 MPa/h, respectively. Hence, hydrogen atoms located in the surroundings of the notch region, driven by the high hydrostatic stress [11], have more time to diffuse up to the so-called embrittled process zone where a critical concentration seems to be reached after 1.3–1.5 h testing. The maximum embrittlement was noted for a loading rate of 63 MPa/h. In this case, the embrittled region attained a total maximum depth of 150 μm (Fig. 13a), mainly characterized by CMD micromechanism.

Fig. 14 shows the fracture surface observed near the notched region for the two analyzed PAGS (i.e. BS and CGHAZ grades) at the maximum embrittlement level. As mentioned, hydrogen damage was particularly observed near the notch tip region, being especially marked in the CGHAZ (Fig. 14b). In the CGHAZ grade, a first belt, with 80 μm depth, was clearly identified. In this area, plasticity-

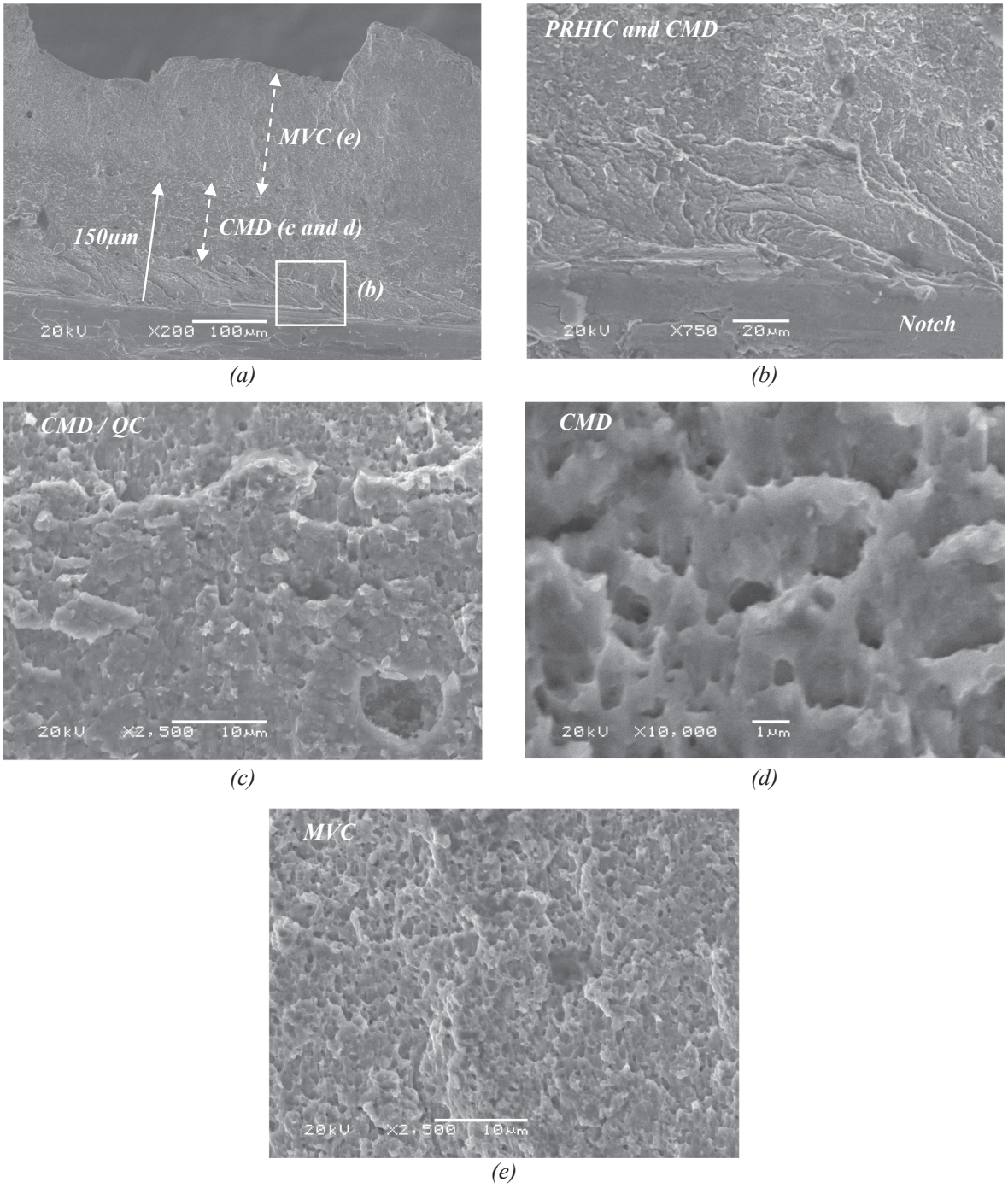

Fig. 13. Hydrogen precharged specimen and testes at 63 MPa/h. (a) General fracture surface appearance. (b) Fracture surface near the notch region with. (c) and (d) Carbide matrix decohesion interfaces. (e) Coalescence of microvoids. 42CrMo4 steel with a PAGS of 20 μm (BS grade).

related hydrogen induced cracking led to ductile micro-plastic tearing decohesion along the martensitic packets, blocks an laths interfaces. Nevertheless, the mentioned ductile micro-plastic tearing decohesion were not clearly identified in the BS grade under the employed magnifications in the SEM.

We postulate there are two main reasons that explain why reducing PAGS improves hydrogen embrittlement resistance. First, reducing the PAGS decreases the hydrogen mobility ($D_{app} \approx 3{\cdot}10^{-11}$ m^2/s) through the steel microstructure (Table 4). In this case, the higher density of traps ($N_T \approx 5{\cdot}10^{24}$ sites/m^3) is mainly associated to hydrogen trapped along HAGBs (and also the one trapped at vacancies and dislocations accumulated at HAGBs), with a fitted binding energy of 45 kJ/mol. These microstructural singularities act

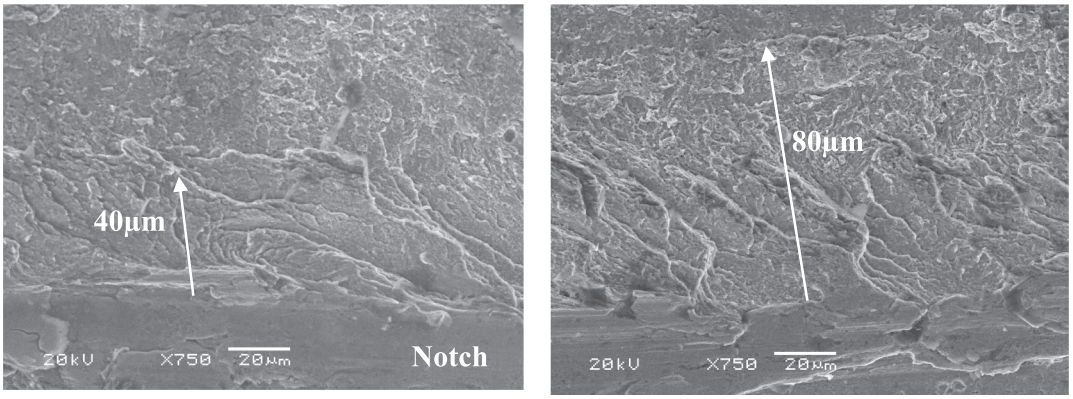

Test duration=1.5h
EI NMOD=17% and EI P_b =18%

Test duration=1.9h
EI NMOD=50% and EI P_b =28%

Fig. 14. Fracture surface features comparison when the embrittlement is maximum. (a) PAGS 20 µm (BS grade) and (b) PAGS 150 µm (CGHAZ grade).

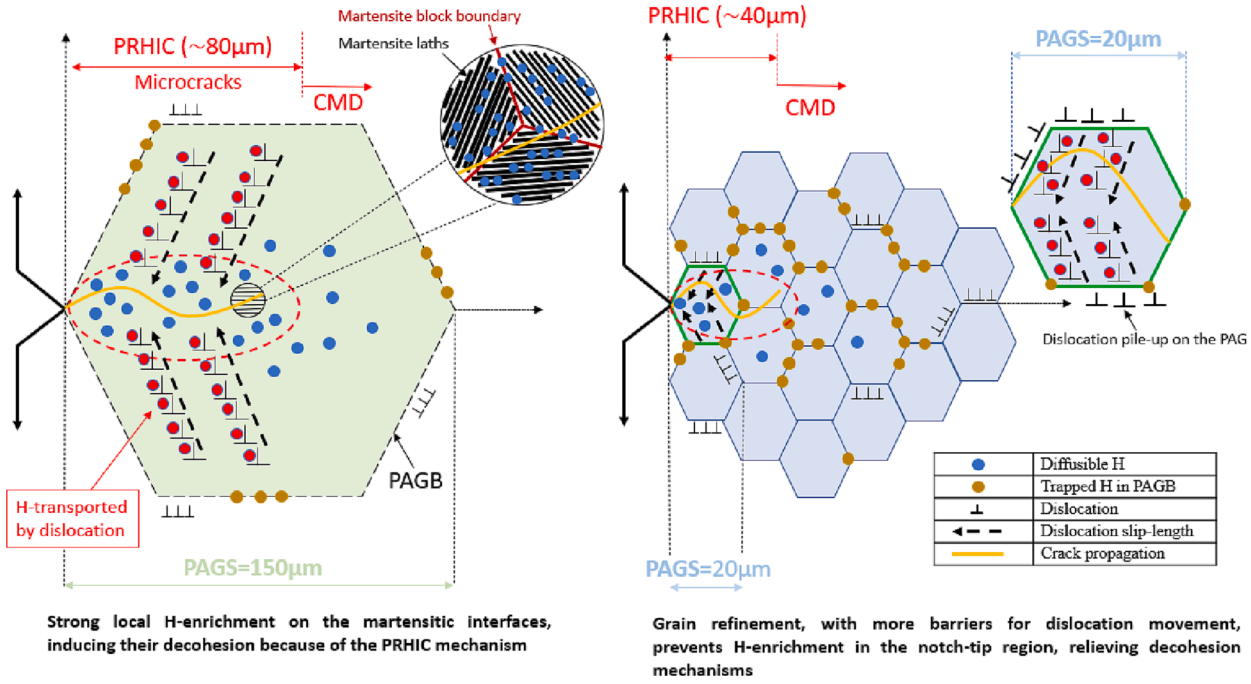

Fig. 15. Hydrogen damage mechanisms in CGHAZ and BS.

as strong traps for hydrogen, preventing hydrogen from reaching potential crack initiation sites [50]. The lower diffusible hydrogen percentage (72%) presented by the BS grade (Table 4) agrees with this statement. This means that a lower amount of hydrogen is able to diffuse to the crack initiation sites, despite the higher initial hydrogen concentration (1.67 wt ppm).

Second, reducing PAGS decreases the slip-length of dislocations [46] Specifically, grain boundaries block dislocation movement, and therefore, grain size refinement is a key factor to prevent dislocation-induced hydrogen transport. Hence, decohesion mechanisms induced by PRHIC are partially mitigated, preventing hydrogen accumulation in the so-called embrittled region. This fact is clearly evidenced in Fig. 14 when BS (a) and CGHAZ (b) are compared under the maximum embrittlement level.

In BS grade (PAGS – 20 µm), the so-called embrittled region with a depth of 40 µm, occupied around 10% of the total fracture surface. It is important to recall that in this area, micro-plastic tearing decohesion along the martensitic packets, blocks an laths interfaces were not clearly identified. However, in the CGHAZ grade (PAGS – 150 µm), the so-called embrittled region increased to 80 µm depth, and it occupied 30% of the total fracture surface. Fig. 15 evidences the main cracking mechanisms in this study.

The CGHAZ grade, with larger PAGS, has larger martensite blocks and less barriers for dislocation movement. Hence, hydrogen transported by dislocation can contribute to induce local hydrogen enrichment on the martensitic laths, blocks and packets interfaces,

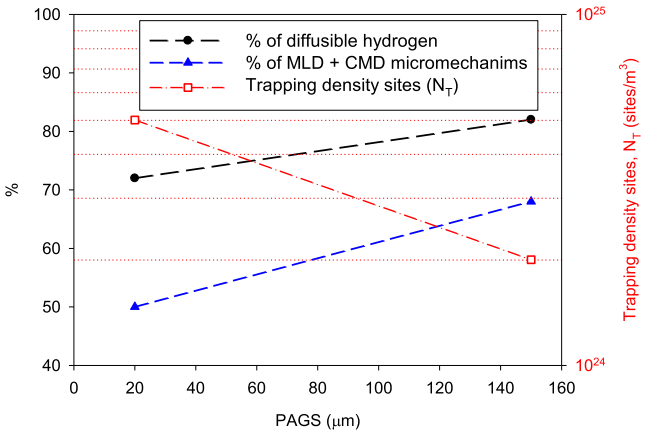

Fig. 16. Interaction H-microstructure with % of MLD (PRHIC) + CMD micromechanisms found for the maximum embrittlement case.

lowering its cohesive energy. Based on hydrogen-enhanced dislocation mobility and density, dislocation transport can contribute to the elevation of the local hydrogen concentration in the crack tip region [51]. Consequently, hydrogen-enhanced decohesion mechanisms were especially marked on the CGHAZ grade, contributing to explain the hydrogen-induced failure and then, the highest embrittlement indexes. Finally, Fig. 16 evidences that trapping capability increases with grain refinement, what seems to contribute to reduce the percentage of hydrogen-enhanced decohesion failure. In this regard, Park et al [34] also reported a significant decrease in the fraction of decohesion fractures with a decrease in the grain size. Unlike what has been observed in [32,34,38] where intergranular fracture was noted in coarser grain structures, in this study, intergranular fracture was not observed. This fact could be explain due to the employed tempering temperature after quenching. This steel (BS and CGHAZ) was tempered at 700 °C for 2 h and then, it has sufficiently relaxed microstructure to induce intergranular fracture, what was also evidenced in [12] for a yield strength of 400–700 MPa.

4. Conclusions

Results of the present work support the following conclusions regarding the hydrogen desorption kinetics, trapping and embrittlement under high internal pressure hydraulic fracture tests of a 42CrMo4 steel with a PAGS of 20 μm (BS) and 150 μm (CGHAZ), respectively:

Despite having a greater initial hydrogen concentration, diffusible hydrogen percentage decreased with grain refinement. This behavior was mainly attributed to hydrogen trapped along the high angle grain boundaries. HAGBs seem to act as effective hydrogen trapping sites, with a binding energy of 45 kJ/mol, preventing hydrogen diffusion through the steel microstructure. Irreversible hydrogen content and trapping density sites increased whilst hydrogen diffusion coefficient considerably decreased after grain refinement.

Hydrogen precharging decreased notably the burst pressure, being this effect especially marked on the simulated CGHAZ grade. This grade with a lower density of traps and a higher hydrogen diffusion coefficient had a higher percentage of diffusible hydrogen. Besides, hydrogen transport by dislocations finds less barriers for movement because of the higher PAGS. Therefore, greater local H-enrichment is assumed to be attained in the notch-tip region, leading to martensitic units interfaces decohesion (MLD) and carbides-matrix interfaces decohesion (CMD).

CRediT authorship contribution statement

L.B. Peral: Conceptualization, Data curation, Writing – original draft, Writing – review & editing, Visualization, Investigation, Formal analysis, Methodology. **A. Díaz:** Writing – review & editing, Writing – original draft, Visualization, Software, Methodology, Investigation, Formal analysis, Conceptualization. **V. Arniella:** Investigation, Data curation. **J. Belzunce:** Validation, Supervision, Resources, Project administration, Funding acquisition. **J.M. Alegre:** Validation, Supervision, Resources, Project administration, Funding acquisition. **I.I. Cuesta:** Validation, Supervision, Resources, Project administration, Methodology, Investigation, Funding acquisition, Conceptualization.

Declaration of Competing Interest

The authors declare that they have no known competing financial interests or personal relationships that could have appeared to influence the work reported in this paper.

Data availability

Data will be made available on request.

Acknowledgments

The authors would like to thank the Spanish Government for the financial support received to perform the research projects TED2021-130413B-I00 and PID2021-124768OB-C21. This work was supported by the Regional Government of Castilla y León (Junta de Castilla y León) and by the Ministry of Science and Innovation MICIN and the European Union Next Generation EU/PRTR (MR5W.P3) and PRTR (MR4W.P2). L.B. Peral is grateful for his Margarita Salas Postdoctoral contract (Ref.: MU-21-UP2021-030) funded by the University of Oviedo through the Next Generation European Union.

References

[1] Murakami Y, Matsuoka S. Effect of hydrogen on fatigue crack growth of metals. Eng Fract Mech 2010;77:1926–40. https://doi.org/10.1016/j.engfracmech.2010.04.012.
[2] Li H, Niu R, Li W, Lu H, Cairney J, Chen YS. Hydrogen in pipeline steels: Recent advances in characterization and embrittlement mitigation. J Nat Gas Sci Eng 2022:105. https://doi.org/10.1016/j.jngse.2022.104709.
[3] Timmerberg S, Kaltschmitt M. Hydrogen from renewables: Supply from North Africa to Central Europe as blend in existing pipelines – Potentials and costs. Appl Energy 2019;237:795–809. https://doi.org/10.1016/j.apenergy.2019.01.030.
[4] Nguyen TT, Park JS, Kim WS, Nahm SH, Beak UB. Environment hydrogen embrittlement of pipeline steel X70 under various gas mixture conditions with in situ small punch tests. Mater Sci Engng A 2020:781. https://doi.org/10.1016/j.msea.2020.139114.
[5] Hua Z, Zhang X, Zheng J, Gu C, Cui T, Zhao Y, et al. Hydrogen-enhanced fatigue life analysis of Cr–Mo steel high-pressure vessels. Int J Hydrogen Energy 2017;42(16):12005–14.
[6] Matsunaga H, Yoshikawa M, Kondo R, Yamabe J, Matsuoka S. Slow strain rate tensile and fatigue properties of Cr-Mo and carbon steels in a 115 MPa hydrogen gas atmosphere. Int J Hydrogen Energy 2015;40:5739–48. https://doi.org/10.1016/j.ijhydene.2015.02.098.
[7] Alazemi J, Andrews J. Automotive hydrogen fuelling stations: An international review. Renew Sustain Energy Rev 2015;48:483–99. https://doi.org/10.1016/j.rser.2015.03.085.
[8] Macadre A, Artamonov M, Matsuoka S, Furtado J. Effects of hydrogen pressure and test frequency on fatigue crack growth properties of Ni–Cr–Mo steel candidate for a storage cylinder of a 70MPa hydrogen filling station. Eng Fract Mech 2011;78:3196–211. https://doi.org/10.1016/j.engfracmech.2011.09.007.
[9] Tsay LW, Liu CC, Chao Y-H, Shieh YH. Fatigue crack propagation in 2.25 Cr–1.0Mo steel weldments in air and hydrogen. Mater Sci Engng A 2001;299:16–26. https://doi.org/10.1016/S0921-5093(00)01420-9.
[10] Zhang T, Zhao W, Deng Q, Jiang W, Wang Y, Wang Y, et al. Effect of microstructure inhomogeneity on hydrogen embrittlement susceptibility of X80 welding HAZ under pressurized gaseous hydrogen. Int J Hydrogen Energy 2017;42(39):25102–13.
[11] Peral LB, Díaz A, Arniella V, Belzunce J, Alegre J, Cuesta II. Hydraulic fracture behavior in the presence of hydrogen in notched miniature cylindrical specimens of a 42CrMo4 steel. Eng Fract Mech 2022:274. https://doi.org/10.1016/j.engfracmech.2022.108749.
[12] Peral LB, Zafra A, Belzunce J, Rodríguez C. Effects of hydrogen on the fracture toughness of CrMo and CrMoV steels quenched and tempered at different temperatures. Int J Hydrogen Energy 2019;44:3953–65. https://doi.org/10.1016/j.ijhydene.2018.12.084.
[13] Arniella V, Zafra A, Álvarez G, Belzunce J, Rodríguez C. Comparative study of embrittlement of quenched and tempered steels in hydrogen environments. Int J Hydrogen Energy 2022;47:17056–68. https://doi.org/10.1016/j.ijhydene.2022.03.203.
[14] Zafra A, Álvarez G, Belzunce J, Rodríguez C. Influence of tempering time on the fracture toughness of hydrogen pre-charged 42CrMo4 steel. Theor Appl Fract Mech 2022;117:103197. https://doi.org/10.1016/j.tafmec.2021.103197.
[15] Peral LB, Zafra A, Blasón S, Rodríguez C, Belzunce J. Effect of hydrogen on the fatigue crack growth rate of quenched and tempered CrMo and CrMoV steels. Int J Fatigue 2019;120:201–14. https://doi.org/10.1016/j.ijfatigue.2018.11.015.
[16] Colombo C, Fumagalli G, Bolzoni F, Gobbi G, Vergani L. Fatigue behavior of hydrogen pre-charged low alloy Cr–Mo steel. Int J Fatigue 2016;83:2–9. https://doi.org/10.1016/j.ijfatigue.2015.06.002.
[17] Wei FG, Hara T, Tsuzaki K. Precise Determination of the Activation Energy for Desorption of Hydrogen in Two Ti-Added Steels by a Single Thermal-Desorption Spectrum. n.d.
[18] Shi R, Ma Y, Wang Z, Gao L, Yang X-S, Qiao L, et al. Atomic-scale investigation of deep hydrogen trapping in NbC/α-Fe semi-coherent interfaces. Acta Mater 2020;200:686–98.
[19] Wallaert E, Depover T, Arafin M, Verbeken K. Thermal Desorption Spectroscopy Evaluation of the Hydrogen-Trapping Capacity of NbC and NbN Precipitates. Metall Mater Trans A 2014;45(5):2412–20.
[20] Frappart S, Feaugas X, Creus J, Thebault F, Delattre L, Marchebois H. Study of the hydrogen diffusion and segregation into Fe–C–Mo martensitic HSLA steel using electrochemical permeation test. J Phys Chem Solid 2010;71:1467–79. https://doi.org/10.1016/j.jpcs.2010.07.017.
[21] Li D, Gangloff RP, Scully JR. Hydrogen Trap States in Ultrahigh-Strength AERMET 100 Steel. n.d.
[22] Nagao A, Smith CD, Dadfarnia M, Sofronis P, Robertson IM. The role of hydrogen in hydrogen embrittlement fracture of lath martensitic steel. Acta Mater 2012;60:5182–9. https://doi.org/10.1016/j.actamat.2012.06.040.
[23] Moshtaghi M, Loder B, Safyari M, Willidal T, Hojo T, Mori G. Hydrogen trapping and desorption affected by ferrite grain boundary types in shielded metal and flux-cored arc weldments with Ni addition. Int J Hydrogen Energy 2022;47:20676–83. https://doi.org/10.1016/j.ijhydene.2022.04.260.
[24] Pérez Escobar D, Depover T, Duprez L, Verbeken K, Verhaege M. Combined thermal desorption spectroscopy, differential scanning calorimetry, scanning electron microscopy and X-ray diffraction study of hydrogen trapping in cold deformed TRIP steel. Acta Mater 2012;60:2593–605. https://doi.org/10.1016/j.actamat.2012.01.026.
[25] Peral LB, Zafra A, Fernández-Pariente I, Rodríguez C, Belzunce J. Effect of internal hydrogen on the tensile properties of different CrMo(V) steel grades: Influence of vanadium addition on hydrogen trapping and diffusion. Int J Hydrogen Energy 2020;45:22054–79. https://doi.org/10.1016/j.ijhydene.2020.05.228.
[26] Asahi H, Hirakami D, Yamasaki S. Hydrogen Trapping Behavior in Vanadium-added Steel. ISIJ Int 2003;43:527–33. https://doi.org/10.2355/isijinternational.43.527.
[27] Zafra A, Peral LB, Belzunce J. Hydrogen diffusion and trapping in A 42CrMo4 quenched and tempered steel: Influence of tempering temperature. Int J Hydrogen Energy 2020;45:31225–42. https://doi.org/10.1016/j.ijhydene.2020.08.134.
[28] Shi R, Chen L, Wang Z, Yang X-S, Qiao L, Pang X. Quantitative investigation on deep hydrogen trapping in tempered martensitic steel. J Alloys Compd 2021;854:157218. https://doi.org/10.1016/j.jallcom.2020.157218.
[29] Oudriss A, Fleurentin A, Courlit G, Conforto E, Berziou C, Rébéré C, et al. Consequence of the diffusive hydrogen contents on tensile properties of martensitic steel during the desorption at room temperature. Mater Sci Engng A 2014;598:420–8.
[30] Takasawa K, Ikeda R, Ishikawa N, Ishigaki R. Effects of grain size and dislocation density on the susceptibility to high-pressure hydrogen environment embrittlement of high-strength low-alloy steels. Int J Hydrogen Energy 2012;37:2669–75. https://doi.org/10.1016/j.ijhydene.2011.10.099.

[31] Cho L, Bradley PE, Lauria DS, Connolly MJ, Seo EJ, Findley KO, et al. Effects of hydrogen pressure and prior austenite grain size on the hydrogen embrittlement characteristics of a press-hardened martensitic steel. Int J Hydrogen Energy 2021;46(47):24425–39.
[32] Martiniano GA, Silveira Leal JE, Rosa GS, Bose Filho WW, Piza Paes MT, Franco SD. Effect of specific microstructures on hydrogen embrittlement susceptibility of a modified AISI 4130 steel. Int J Hydrogen Energy 2021;46:36539–56. https://doi.org/10.1016/j.ijhydene.2021.08.147.
[33] Chen S, Zhao M, Rong L. Effect of grain size on the hydrogen embrittlement sensitivity of a precipitation strengthened Fe–Ni based alloy. Mater Sci Engng A 2014;594:98–102. https://doi.org/10.1016/j.msea.2013.11.062.
[34] Park C, Kang N, Liu S. Effect of grain size on the resistance to hydrogen embrittlement of API 2W Grade 60 steels using in situ slow-strain-rate testing. Corros Sci 2017;128:33–41. https://doi.org/10.1016/j.corsci.2017.08.032.
[35] Nakamura M, Furubayashi E. Effect of grain size on crack propagation of high strength steel in gaseous hydrogen atmosphere. Mater Sci Technol 1990;6:604–10. https://doi.org/10.1179/mst.1990.6.7.604.
[36] Lessar JF, Gerberich WW. Grain Size Effects in Hydrogen-Assisted Cracking. Metall Trans A 1976;7:953–60. https://doi.org/10.1007/BF02644060.
[37] Bhadeshia HKDH. Prevention of hydrogen embrittlement in steels. ISIJ Int 2016;56:24–36. https://doi.org/10.2355/isijinternational.ISIJINT-2015-430.
[38] Zafra A, Belzunce J, Rodríguez C, Fernández-Pariente I. Hydrogen embrittlement of the coarse grain heat affected zone of a quenched and tempered 42CrMo4 steel. Int J Hydrogen Energy 2020;45:16890–908. https://doi.org/10.1016/j.ijhydene.2020.04.097.
[39] Filho CJC, Mansur MB, Modenesi PJ, Gonzalez BM. The effect of hydrogen release at room temperature on the ductility of steel wire rods for pre-stressed concrete. Mater Sci Engng A 2010;527:4947–52. https://doi.org/10.1016/j.msea.2010.04.042.
[40] Sofronis P, McMeeking RM. Numerical analysis of hydrogen transport near a blunting crack tip. J Mech Phys Solids 1989;37:317–50. https://doi.org/10.1016/0022-5096(89)90002-1.
[41] Dadfarnia M, Sofronis P, Neeraj T. Hydrogen interaction with multiple traps: Can it be used to mitigate embrittlement? Int J Hydrogen Energy 2011;36:10141–8. https://doi.org/10.1016/j.ijhydene.2011.05.027.
[42] Peral LB, Amghouz Z, Colombo C, Fernández-Pariente I. Evaluation of hydrogen trapping and diffusion in two cold worked CrMo(V) steel grades by means of the electrochemical hydrogen permeation technique. Theor Appl Fract Mech 2020;110:102771. https://doi.org/10.1016/j.tafmec.2020.102771.
[43] Nagao A, Dadfarnia M, Somerday BP, Sofronis P, Ritchie RO. Hydrogen-enhanced-plasticity mediated decohesion for hydrogen-induced intergranular and "quasi-cleavage" fracture of lath martensitic steels. J Mech Phys Solids 2018;112:403–30. https://doi.org/10.1016/j.jmps.2017.12.016.
[44] Yazdipour N, Haq AJ, Muzaka K, Pereloma EV. 2D modelling of the effect of grain size on hydrogen diffusion in X70 steel. Comput Mater Sci 2012;56:49–57. https://doi.org/10.1016/j.commatsci.2012.01.003.
[45] Zhang D, Gao X, Du Yu, Du L, Wang H, Liu Z, et al. Effect of microstructure refinement on hydrogen-induced damage behavior of low alloy high strength steel for flexible riser. Mater Sci Engng A 2019;765. https://doi.org/10.1016/j.msea.2019.138278.
[46] Fuchigami‡ H, Minami§ H, Nagumo‖ M. Effect of grain size on the susceptibility of martensitic steel to hydrogen-related failure. Philos Mag Lett 2006;86(1):21–9.
[47] Elkot MN, Sun B, Zhou X, Ponge D, Raabe D. Hydrogen-assisted decohesion associated with nanosized grain boundary κ-carbides in a high-Mn lightweight steel. Acta Mater 2022:241. https://doi.org/10.1016/j.actamat.2022.118392.
[48] Takeda Y, McMahon CJ. Strain controlled vs stress controlled hydrogen induced fracture in a quenched and tempered steel. Metall Trans A 1981;12:1255–66. https://doi.org/10.1007/BF02642339.
[49] Zafra A, Belzunce J, Rodríguez C. Hydrogen diffusion and trapping in 42CrMo4 quenched and tempered steel: Influence of quenching temperature and plastic deformation. Mater Chem Phys 2020:255. https://doi.org/10.1016/j.matchemphys.2020.123599.
[50] Das T, Rajagopalan SK, Brahimi SV, Wang X, Yue S. A study on the susceptibility of high strength tempered martensite steels to hydrogen embrittlement (HE) based on incremental step load (ISL) testing methodology. Mater Sci Engng A 2018;716:189–207.
[51] Dadfarnia M, Martin ML, Nagao A, Sofronis P, Robertson IM. Modeling hydrogen transport by dislocations. J Mech Phys Solids 2014;78:511–25. https://doi.org/10.1016/j.jmps.2015.03.002.